The segregation of recycled basaltic material within mantle plumes explains the detection of the X-Discontinuity beneath hotspots: 2D geodynamic simulations

Martina Monaco[1], Juliane Dannberg[1], Rene Gassmoeller[1], Stephen Pugh[2]

[1]University of Florida, Department of Geological Sciences, 241 Williamson Hall, 32611, Gainesville, FL
[2]Bullard Laboratories, Department of Earth Sciences, University of Cambridge, United Kingdom

Key Points:

- Plumes can carry enough basaltic material to explain observations of the X-discontinuity at 300 km depth
- Accounting for the dynamics of individual chemical heterogeneities allows the accumulation of more basalt than previously thought possible
- Near phase transitions, the local basalt fraction of plumes carrying 10-20% of basalt on average can temporarily reach more than 40%

Corresponding author: Martina Monaco, martinamonaco@ufl.edu

Abstract

Mantle plumes are thought to recycle material from the Earth's deep interior. One constraint on the nature and quantity of this recycled material comes from the observation of seismic discontinuities. The detection of the X-discontinuity beneath Hawaii, interpreted as the coesite-stishovite transition, requires the presence of at least 40% basalt. However, previous geodynamic models have predicted that the percentage of high-density basaltic material that mantle plumes can carry to the surface is no higher than 15–20%.

We propose this contradiction can be resolved by taking into account the length scale of chemical heterogeneities. While previous modeling studies assumed mechanical mixing on length scales smaller than the model resolution, we here model basaltic heterogeneities with length scales of 30–40 km, allowing for their segregation relative to the pyrolitic background plume material. Our models show that larger basalt fractions than previously thought possible—exceeding 40%—can accumulate within plumes at the depth of the X-discontinuity. Two key mechanisms facilitate this process: (1) The random distribution of basaltic heterogeneities induces large temporal variations in the basalt fraction with cyclical highs and lows. (2) The high density contrast between basalt and pyrolite below the coesite-stishovite transition causes ponding and accumulation of basalt at that depth, an effect that only occurs for intermediate viscosities of pyrolite.

These results further constrain the chemical composition of the Hawaiian plume. Beyond that, they provide a geodynamic mechanism that explains the seismologic detection of the X-discontinuity and highlights how recycled material is carried towards the surface.

Plain Language Summary

Mantle plumes are thought to cause hotspot magmatism. Around 300 km beneath the Hawaiian hotspot, seismologic studies identified a jump in seismic velocities named the 'X-discontinuity'. This feature is only observed at specific locations and is interpreted to be the result of a transformation in the quartz minerals in basaltic rocks.

For the X-discontinuity to be seismically visible, basalt fractions of 40% or more are required around 300 km depth. However, previous studies found that plumes can not carry more than 15-20% of heavier basaltic material. To overcome this contradiction, we create a series of models featuring a section of the plume and the basaltic material carried within it. In contrast to existing studies, we model the basaltic heterogeneities as individual inclusions that can move upwards or downwards with respect to the plume, rather than assuming that the basalt and the plume material are well-mixed.

We find that depending on the plume viscosity, basaltic material can pond and accumulate above and around 410 km depth, reaching peak fractions of more than 40%. Our models show how larger fractions of basaltic material than previously thought can accumulate within plumes in the upper mantle, thus reconciling the observations of the X-discontinuity.

1 Introduction

Geodynamic studies have long acknowledged the thermochemical nature of mantle plumes (Ballmer et al., 2013; Dannberg & Sobolev, 2015; Jellinek & Manga, 2004; Lin & van Keken, 2006; Lin & Van Keken, 2006). Several lines of evidence (e.g. A. V. Sobolev et al., 2005, 2007; S. V. Sobolev et al., 2011) indicate that recycled subducted eclogitic material is entrained (Christensen & Hofmann, 1994; Tackley, 2007) and eventually brought to the surface by rising plumes.

Eclogite is denser than the surrounding mantle. Therefore, its entrainment critically influences plume dynamics in a number of ways that include: slowing down or even halting plume ascent (Dannberg & Sobolev, 2015; Lin & van Keken, 2006; Samuel & Bercovici, 2006), increasing the thickness of the plume conduit (Dannberg & Sobolev, 2015; Kumagai et al., 2008), and facilitating an asymmetric plume shape deviating from the classical head–tail structure (Ballmer et al., 2013; Farnetani & Samuel, 2005). However, since only a fraction of the recycled material makes it to the surface, very few constraints exist on the amount of denser recycled material that remains in the mid-mantle.

Some of these important constraints come from seismology. The presence of additional mineral phases has been linked to the local appearance of additional seismic discontinuities in the mantle. One such discontinuity is the X-discontinuity, which has been observed in the mid-upper mantle ($\sim$300 km depth) across a variety of tectonic settings, including subduction zones (Revenaugh & Jordan, 1991; Schmerr et al., 2013), hotspots (Kemp et al., 2019; Pugh et al., 2021), and mid-ocean ridges (Schmerr et al., 2013). The X-discontinuity is seismically $<$5 km thick (Revenaugh & Jordan, 1991; Bagley & Revenaugh, 2008; Pugh et al., 2021), with an impedance contrast of 3–8% (Schmerr et al., 2013; Chen et al., 2017; Bagley & Revenaugh, 2008). Its enigmatic occurrence is commonly attributed to two mineral phase transitions. One such phase transition occurs in the crystal structure of (Mg,Fe)SiO_3 pyroxene (Woodland & Angel, 1997; Woodland, 1998; Jacobsen et al., 2010), which transforms from orthoenstatite to high-pressure clinoenstatite. The other involves the transition from coesite to stishovite occurring in silica minerals (Deuss & Woodhouse, 2002; Williams & Revenaugh, 2005; Bagley & Revenaugh, 2008; Schmerr et al., 2013). The latter produces an impedance contrast of 2–5% (Williams & Revenaugh, 2005) due to its large change in seismic velocities (Chen et al., 2017; Faccenda & Dal Zilio, 2017; Williams & Revenaugh, 2005). In order for the Co–St phase transition to occur, enough free silica needs to be available. Eclogite, which is the stable mineral assemblage of basaltic material under the pressure and temperature conditions around 300 km depth in the mantle (Aoki & Takahashi, 2004; Faccenda & Dal Zilio, 2017), is often assumed to be this source of silica.

Mineral physics studies show that in models where the mantle composition is modeled as a mechanical mixture of basalt and harzburgite, stishovite is present regardless of the basalt fraction in the mantle, and the X-discontinuity appears (Xu et al., 2008). Conversely, stishovite is not present in an equilibrium assemblage where the mantle is assumed to be pyrolitic in composition, unless basalt fractions are very large (around or above 70%) (Xu et al., 2008). From a geodynamics perspective, these findings mean we can use the occurrence of the X-discontinuity to constrain the amount of basalt that is present as a separate chemical phase in mantle plumes.

The Hawaiian hotspot is a prominent example of mantle plume activity, where both the seismic properties of the mantle and the geochemistry of the magmatic products have been extensively investigated. Geochemical constraints (Eiler et al., 1996; Hauri, 1996; Hofmann & White, 1982; A. V. Sobolev et al., 2005, 2007) indicate the presence of a substantial component of recycled basaltic crust in the plume. Several seismic studies (Courtier et al., 2007; Kemp et al., 2019) have detected the X-discontinuity beneath Hawaii using receiver functions and ScS reverberations. Kemp et al. (2019) observed the X-discontinuity beneath Big Island at around 300 km depth, finding a deeper, stronger signal beneath the eastern part of the island. In the same area, their results show a very weak signal from the 410 km discontinuity. They suggest that percentages of basaltic material between 40–50% are required to explain the occurrence of the X-discontinuity, and up to 60-70% of eclogite is required to cause the disappearance of the 410 km discontinuity.

However, geodynamic studies (Dannberg & Sobolev, 2015) predict that a plume can carry no more than 15–20% dense eclogitic material to the surface. Models show that higher fractions of recycled basalt would render the plume negatively buoyant, causing it to stall in the deep mantle or transition zone and thus to never reach the surface.

To resolve the discrepancy between these different lines of evidence, we model the accumulation of eclogitic material within a mantle plume conduit. In particular, we focus on the depth range between 300 and 410 km, where the density difference between eclogite and the average mantle is especially large (Aoki & Takahashi, 2004; Stixrude & Lithgow-Bertelloni, 2011). Consequently, plumes carrying eclogite might slow down or even halt their ascent in this depth range (Ballmer et al., 2013; Dannberg & Sobolev, 2015), but the high density contrast can also facilitate ponding of eclogitic material in a so-called Deep Eclogitic Pool (Ballmer et al., 2013). Here, we investigate whether this increased density contrast can provide a mechanism for the plume material to accumulate up to ≈40% eclogite — the fraction needed to explain the appearance of the X-discontinuity in seismic studies.

We set up a series of geodynamic models featuring a pyrolitic background — representing a section of a plume conduit — and higher density chemical heterogeneities flowing in, representing the eclogitic recycled material. To do so, we adopt a new approach of modeling the motion of chemical heterogeneities. Most existing studies assume that mechanical mixing of the different chemical components occurs on a length scale below the model resolution and that accordingly, the components in the mixture all move at the same velocity. Instead, we model the recycled material as having a larger length scale than the model resolution. This means that the basaltic heterogeneities can move upwards or downwards within the plume conduit at a different velocity to the plume as a whole. Because the density contrast between the different chemical components varies with depth, this can allow for basaltic material to segregate and to accumulate to higher fractions than carried by the plume on average. We perform 230 model runs, employing three different density profiles, a range of background viscosities between 10^{18}–10^{21} Pa s, and five different inflow percentages of recycled material.

Our models predict the conditions under which chemical heterogeneities can pond in plumes and provide an upper limit for the eclogite fractions that can accumulate. These results link plume heterogeneity to the local occurrence of the X-discontinuity beneath some hotspots, shedding light on the underlying mechanisms behind its appearance and allowing us to better constrain the Hawaiian plume composition.

2 Model setup

To model the plume conduit, we developed geodynamic models employing the mantle convection code ASPECT (Kronbichler et al., 2012; Heister et al., 2017; Bangerth et al., 2021a, 2021b). ASPECT is a parallel, modular, open source, finite-element code written in C++. It is based on three libraries: *deal.II*, a general-purpose finite element library (Arndt et al., 2021), *Trilinos*, which performs linear algebra computations (Trilinos Project Team, n.d.; Kronbichler et al., 2012), and *p4est*, which handles the adaptive meshes (Burstedde et al., 2011).

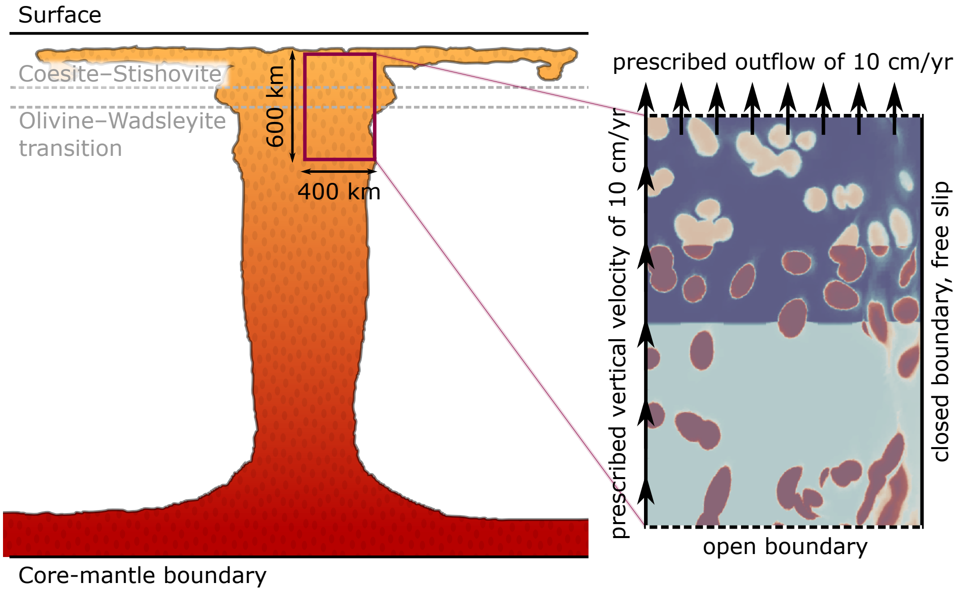

Figure 1. Model setup and boundary conditions. We model a section of the plume conduit in the upper mantle, including the Co–St transition at 300 km and the Ol–Wd transition at 410 km depth. Red and orange blobs represent chemical heterogeneities.

2.1 Basic equations

Over geologic timescales, the Earth's mantle behaves like a viscous, slow-moving fluid (Schubert et al., 2001) whose convection can be described using the Stokes equations that state the conservation of mass (Equation 2) and momentum (Equation 1). We formulate these equations using the Boussinesq approximation, assuming that the material is incompressible and neglecting all density variations except for the buoyancy term $\rho\mathbf{g}$ in the momentum equation (Schubert et al., 2001; van Zelst et al., 2021).

$$-\nabla \cdot [2\eta\dot{\varepsilon}'] + \nabla p = \rho\mathbf{g} \tag{1}$$

$$\nabla \cdot \mathbf{u} = 0 \tag{2}$$

Here, $\mathbf{u}$ is the velocity, η the viscosity, $\dot{\varepsilon}'$ the deviatoric strain rate tensor defined as $\dot{\varepsilon}' = \frac{1}{2}(\nabla\mathbf{u} + (\nabla\mathbf{u})^T)$, p the pressure, ρ the density, and $\mathbf{g}$ the gravity.

Since we do not take into account the effects of temperature, we do not solve the energy conservation equation. On the other hand, our models include chemical heterogeneities in the form of spherical basaltic inclusions within a pyrolitic matrix. The transport of the basaltic material can be described by the following advection equation:

$$\frac{\partial C}{\partial t} + \mathbf{u} \cdot \nabla C = 0, \tag{3}$$

with t being the time and C the composition, which in our case represents the basalt (eclogite) fraction. The fraction of the background pyrolite is then obtained as $1 - C$. We solve this advection problem adopting the particle-in-cell method (Gassmöller et al., 2018, 2019). Particles are generated at random locations at the start of the model run, and in cells where material enters the model. The initial composition of each particle is an input parameter, which we specify according to the initial conditions or boundary conditions (see Section 2.4). To interpolate composition from the particle locations to the grid points, we employ a cell-wise constant averaging operation.

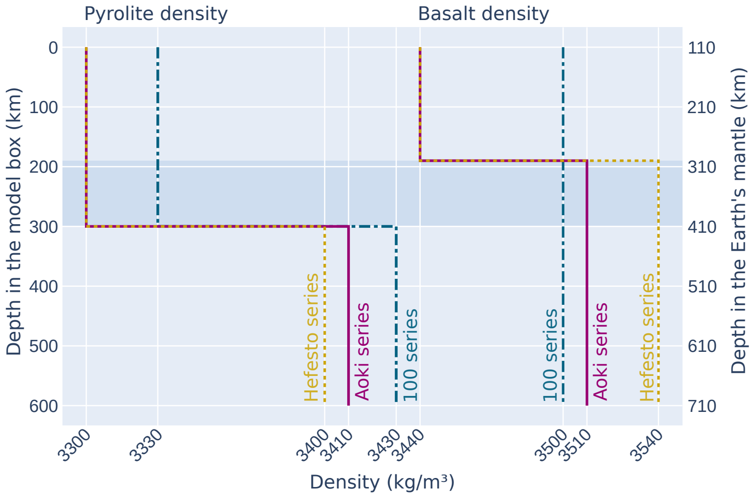

Figure 2. Density profiles for the three series. The left y-axis shows the depth in the model box, while the right y-axis refers to the real mantle depth. The curves on the left show the density distribution for the background pyrolite, while the right-hand side shows the values for the basaltic chemical heterogeneities. The sharp jumps in pyrolite density correspond to the Ol–Wd phase transition at 410 km depth. The density increase in the basaltic material is associated with the Co–St phase transition at 300 km depth (only included in the Aoki and Hefesto series).

Particle motion is computed using a second-order Runge-Kutta advection scheme. In order to make sure there are always enough particles for an accurate solution without unreasonably increasing the computational time, we impose a minimum of 10 and maximum number of 15 particles per cell.

2.2 Model geometry

The model setup consists of a 2D box, 400 km in width and 600 km in depth, representing a section of the plume conduit (Figure 1). The top of the box is located at 110 km depth in the Earth's mantle, since the model does not include the lithosphere.

To resolve the chemical heterogeneities, which have a diameter between 30 and 40 km, we use an adaptive mesh to discretize the domain (Bangerth et al., 2021b), varying the cell size from 1.56–25 km through global and adaptive refinements. This strategy allows us to selectively resolve the smallest features in the model, as the mesh is refined only at locations where additional precision is needed (Gassmöller et al., 2018; Kronbichler et al., 2012). Specifically, we use the highest resolution where we estimate the error of the composition C to be large (based on the Kelly error estimator, Kronbichler et al., 2012) and at the bottom boundary where material flows in. This is required to make sure that the chemical heterogeneities are resolved as they enter the box.

2.3 Density profiles

We test three different density profiles in our models. All profiles include the olivine–wadsleyite (Ol–Wd) phase transition, which occurs at 410 km depth in the mantle. Relative to our model box, this depth corresponds to 300 km (as we do not include the lithosphere), which allows us to model two equal-sized halves with different densities (see Figure 2, left-hand curves).

The three profiles differ in terms of the basalt density distribution (Figure 2, right-hand curves). We include one profile (the 100 series) that features a uniform basalt density of 3500 kg/m^3 and a pyrolite density jump of 100 kg/m^3 at the Ol–Wd transition. In this series, the density difference between basalt and pyrolite increases from 70 kg/m^3 below the 410 km depth phase transition to 170 kg/m^3 above the phase transition. The 100 series is our simplest case, and we use it to analyze the general behavior of the heterogeneities when interacting with phase transitions before testing more complex scenarios.

The Aoki and Hefesto series adopt density values from Aoki and Takahashi (2004) and Stixrude and Lithgow-Bertelloni (2011), respectively. In addition to the Ol–Wd transition, they feature the coesite–stishovite (Co–St) phase transition in the basaltic material at 300 km depth, such that basalt has two different density values above and below (see Figure 2). Below the transition, the Hefesto series features the highest densities of basalt and the lowest densities of pyrolite, while the Aoki series has intermediate values of pyrolite and basalt densities compared to the other two series. Given that the Co–St transition occurs at a shallower depth than the Ol–Wd transition, the density contrast between basalt and pyrolite reaches its largest values in the depth range between 300 and 410 km depth in the mantle (190 to 300 km depth in our model box).

2.4 Boundary and initial conditions

Our model represents a section of an existing plume conduit. Therefore we assume that the material moves upwards within the plume, and that it can move faster in the hot center of the plume (left model boundary) compared to the colder plume margin. Accordingly, we prescribe the following boundary conditions (Figure 1): At the top and left sides, we impose a boundary velocity of 10 cm/yr in vertical direction, and zero in horizontal direction. The right side of the model–representing the plume margin–has an unrestrained velocity tangential to the boundary and a zero velocity normal to the boundary (free slip conditions). The bottom boundary is open and stress-free, so that material can flow in according to the forces acting in the model.

Consequently, our models are driven by the boundary conditions. We do not model the buoyancy forces of the plume itself, but instead assume that the plume is moving upwards with a fixed speed of 10 cm/yr and then investigate how chemical heterogeneities within the plume conduit affect its internal convection.

At the bottom boundary, where material flows into the model, the composition has to be prescribed. Specifically, we assume that the basaltic material is distributed within the plume in the form of circular inclusions at random locations, each with a diameter between 30 and 40 km. The number of basaltic inclusions flowing into the box within a given time is a model parameter that allows us to regulate the average fraction of basalt within the plume (see Section 2.6). No heterogeneities are present in the model at the start time. We let all models evolve for 100 million years, which is long enough for them to reach a steady state.

2.5 Model parameters

In order to analyze our models, we identify which parameters have the strongest influence on the motion of the chemical heterogeneities in the plume using a scaling analysis. This analysis allows us to predict the general physical behaviour of basaltic material in a plume and to select a reasonable parameter range. We assume that the behavior of the heterogeneities with respect to the background pyrolite is governed by three forces: (1) the drag force F_D (equation 4), which can be expressed by the Stokes law for a falling sphere in a laminar flow, (2) the gravitational force F_G (equation 5), and (3) the buoyancy force F_B (equation 6):

$$F_D = 6\pi\eta r v, \tag{4}$$

$$F_G = \frac{4}{3}\pi r^3 \rho_s g, \tag{5}$$

$$F_B = \frac{4}{3}\pi r^3 \rho_b g, \tag{6}$$

with r being the radius of the spherical heterogeneity, v the relative velocity of that sphere with respect to the fluid it moves in, η the viscosity and ρ_b the density of that fluid, ρ_s the sphere density, and g the acceleration due to gravity.

Let us assume that the sphere accelerates until the drag force reaches a point where the net force on the sphere is zero. From that point onward, the sphere moves with a constant velocity, the terminal velocity v_T:

$$v_T = \frac{2r^2(\rho_s - \rho_b)g}{9\eta} \tag{7}$$

v_T is directly proportional to the square of the sphere radius, the density difference between the sphere and the background, and inversely proportional to the background viscosity. This means that in our models, the motion of the heterogeneities is governed by three parameters: the pyrolite viscosity, the density difference between basalt and pyrolite, and the diameter of the heterogeneities.

Given that the basaltic heterogeneities are denser than the pyrolitic background, v_T points downwards relative to the upwards flow within the plume. Consequently, we expect heterogeneities to sink, rise or hover, depending on our model parameters. Because there is a trade-off between these parameters, we can achieve the same regime by either changing the pyrolite viscosity, the density distribution, or the diameter of the spheres. Since the length scale of chemical heterogeneities in the mantle is unknown, we here choose a fixed diameter for the spheres of $30-40$ km, which is enough for us to resolve them individually. This also allows us to observe the three different behaviors described above across a range of pyrolite viscosities that can be reasonably expected within a plume.

Because the density difference between pyrolite and basalt varies with depth, it is possible for the heterogeneities to show a combination of the different behaviors described above. For example, heterogeneities might rise upwards with the plume below 410 km depth, but then sink above 410 km depth, providing a mechanism for basalt to accumulate. To estimate at which conditions the spheres hover above the Ol-Wd phase transition, we can calculate the viscosity where v_T equals 10 cm/yr, the plume velocity we impose. Using the average value of 17.5 km for the sphere radius, a density contrast of 170 kg/m^3 or 70 kg/m^3 (as in the 100 series), and $g = 10$ m/s^2, the resulting background viscosity range where we expect accumulations of basaltic material is $\eta = 1.5...3.7 \times 10^{19}$ Pa s. Note that this is only a rough estimate, since our models are two- instead of three-dimensional and they allow several spheres to interact.

2.6 Model Runs

In addition to using different density profiles (Section 2.3), we also vary the quantity of chemical heterogeneities flowing into the box by setting five influx percentages: 10%, 15%, 20%, 30%, and 40%. These influx percentages correspond to the fraction of recycled material entrained by the plume, and they are implemented by placing spheres at random locations at the inflow boundary with a given probability (see Section 2.4). As a result, some heterogeneities overlap with one another, and the actual influxes are lower than the influx percentages given above, specifically: 9.21%, 14.12%, 17.81%, 25.91%, and 32.86%. In the following, we will therefore refer to the different series by their rounded percentages: 10%, 15%, 20%, 25%, and 35%.

Previous studies (Dannberg & Sobolev, 2015, and references therein) have shown that plumes likely can not carry more than about 15-20% of dense eclogitic material towards the surface, as higher fractions would make them too dense to rise. Consequently, we use the higher basalt influx percentages (25% and 35%) to explore the parameter space, although they are likely not applicable to plumes in the Earth's mantle.

For all three density profiles, we run models with the five influx percentages above and across a range of pyrolite viscosities from 10^{18}–10^{21} Pa s. The viscosity of the basaltic material is always two orders of magnitude larger than the pyrolite viscosity. The relative strength between pyrolite and eclogite in the Earth is uncertain and is expected to vary with temperature and pressure, depending on the stable mineral phases (Farla et al., 2017; Jin et al., 2001). But since eclogite bodies with a lower viscosity would have easily been stirred into the mantle, we here assume that eclogite has the higher viscosity. This prevents excessive deformation of the heterogeneities, especially in models where the pyrolite viscosity is low (Manga, 1996).

3 Results

We analyze the model runs based on the amount of basalt that accumulates around the two phase transitions and test whether basalt fractions as high as 40%, as indicated by seismological observations, are reached around 310 km depth. For the 100 series, which only features the Ol–Wd phase transition, we compute the average basalt fraction between 310 and 510 km depth. For the Aoki and Hefesto series, we take into account the Co–St transition as well, and average the basalt fraction between 260 and 360 km depth. We use these averages to classify the behavior of each model based on the maximum basalt fraction and the maximum root mean square velocity, and additionally analyze the evolution of the basalt fraction over time compared to the basalt influx, highlighting the mechanisms of basalt accumulation. However, we note that using these different depth ranges for computing basalt accumulation in the models affects their statistical properties (see Section 3.2).

3.1 Influence of the viscosity

The behavior of the chemical heterogeneities is first and foremost determined by the pyrolite viscosity. Depending on its value, we identify three different regimes: (1) *sinking*, (2) *mixed*, and (3) *rising*.

The *sinking* regime occurs for the lowest viscosity values and is highlighted in purple in Figures 4 and A1. In this regime, the gravity forces acting on the dense chemical heterogeneities exceed the frictional forces that would allow them to be carried upwards with the plume (see Section 2.5). Therefore, most heterogeneities sink shortly after entering the box. Only a few sparse and elongated strands of basalt rise above the Ol–Wd phase transition at 410 km depth, after undergoing extreme deformation (see Figure 3, top left). This strong deformation, enabled by the low viscosity, is also reflected by the temporally variable and generally very high root mean square velocities. They show values from 0.185 m/yr up to 0.796 m/yr, substantially deviating from the imposed boundary velocity of 0.1 m/yr.

We define a model as belonging to the sinking regime if the maximum basalt percentage is substantially lower or equal to the prescribed inflow percentage. The mean basalt percentages in the sinking regime are: 3.86% for the 100 series, 2.56% for

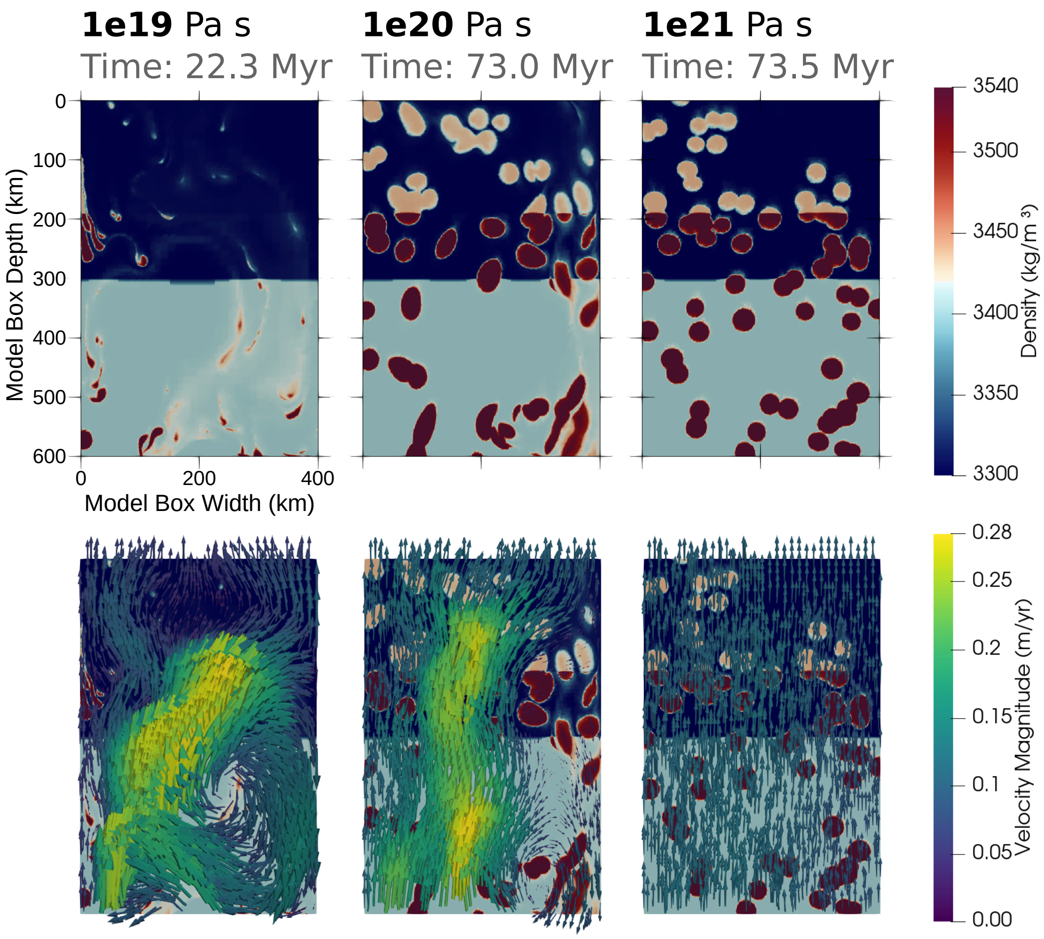

Figure 3. Distribution of the basaltic heterogeneities, as illustrated by the density (top row), and velocities in the model (bottom row) for the three different regimes, which are, left to right: sinking, mixed, and rising. The models shown are from the Hefesto series.

the Aoki series, and 2.11% for the Hefesto series, including the 25% and 35% influx runs.

At the opposite end of the spectrum is the *rising* regime, colored in green in Figures 4 and A1. For this regime, the pyrolite viscosity is so high that all chemical heterogeneities rise with the same velocity as the background (right panel in Figure 3), indicating the absence of deformation. We consequently define this regime based on the root mean square velocity: Whenever its maximum value is below 0.12 m/yr in a model throughout its whole evolution, we define the model as belonging to the rising regime. Regardless of the model series, pyrolite viscosities between 1 and 2×10^{20} Pa s mark the onset of the rising regime. The models belonging to this regime show high maximum basalt fractions, in many cases twice as high as the basalt influx.

We obtain the most noteworthy results for the *mixed* regime, which occurs at intermediate pyrolite viscosities and is highlighted in yellow in Figures 4 and A1. In this regime, the basaltic heterogeneities show a combination of rising and sinking motions. Consequently, heterogeneities cyclically pond around the Ol–Wd transition. This ponding reflects the density contrast between pyrolite and basalt and the associated downwards gravitational force, which is largest between the Co–St and the Ol–Wd transitions (see Section 3.3). Because the friction force stays the same, the heterogeneities can be carried upwards more easily below 410 km and above 300 km depth, but are more likely to sink in between. This makes their ascent path irregular, as they get entrained by the background flow to a variable degree. Therefore, depending on their position with respect to the model boundaries, the phase transition, and the degree of clustering of individual inclusions, they either sink, rise or pond (see Figure 3, center column).

Because basalt cyclically accumulates between 300 and 410 km depth, the fraction of basalt at this depth at times substantially exceeds the average fraction of basalt flowing in at the bottom of the model (Figure 5). The maximum percentages of basalt in the *dynamically consistent* models with basalt inflows up to 20% are between 16% and 43%.

The mixed regime consists of all the models that are neither in the rising nor in the sinking regime. Its lower boundary is determined by the basalt percentages, i.e. when the maximum basalt fraction is higher than the prescribed inflow. The upper boundary instead depends on the velocity, such that all models in the mixed regime reach a root mean square velocity of 0.12 m/yr or more averaged over the depth range of interest at some point throughout the model evolution.

The regime diagrams also show that the boundaries between regimes are not always horizontal lines. This is a direct consequence of the differences caused by the different basalt influx percentages. The chemical heterogeneities modeled here are always two orders of magnitude more viscous than the background. Therefore, the higher the fraction of basaltic material in the box, the higher the average viscosity. Note that basalt inflow fractions of more than 20% are unlikely to be present in plumes in the Earth, which is why we focus our analysis on the three lowest influx percentages only.

3.2 Evolution over time

In addition to analyzing the maximum basalt fraction in each model, it is also useful to look at how the basalt fraction around the phase transitions evolves over time. Figure 5 shows this evolution for three selected models of the Aoki series. The basalt fraction remains low in the sinking regime (blue line), while it varies dramatically over time in the mixed and rising regimes. In these two latter cases (purple and yellow lines), the evolution shows an initial increase in basalt fraction up to 20% as material flows

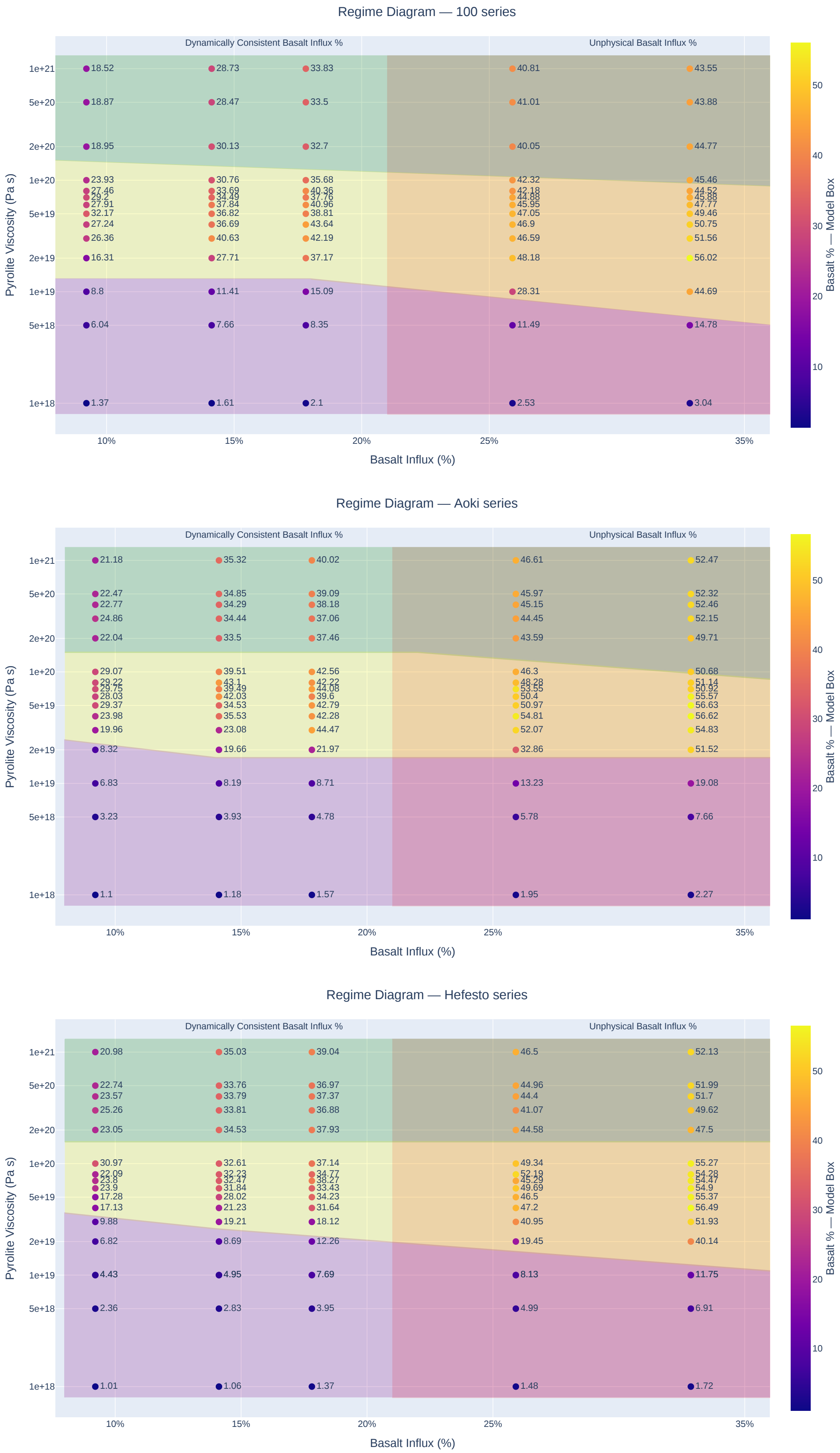

Figure 4. Regime Diagrams for the three series. The shading colors indicate, from bottom to top: the sinking regime (purple), the mixed regime (yellow), and the rising regime (green). The colors of the data points indicate the maximum percentage of basalt attained in the depth layer between 300 and 410 km depth.

in from below. Models in the mixed regime (purple line) then gradually accumulate more basalt, regularly reaching peaks above 30%, and sometimes even 40% or more.

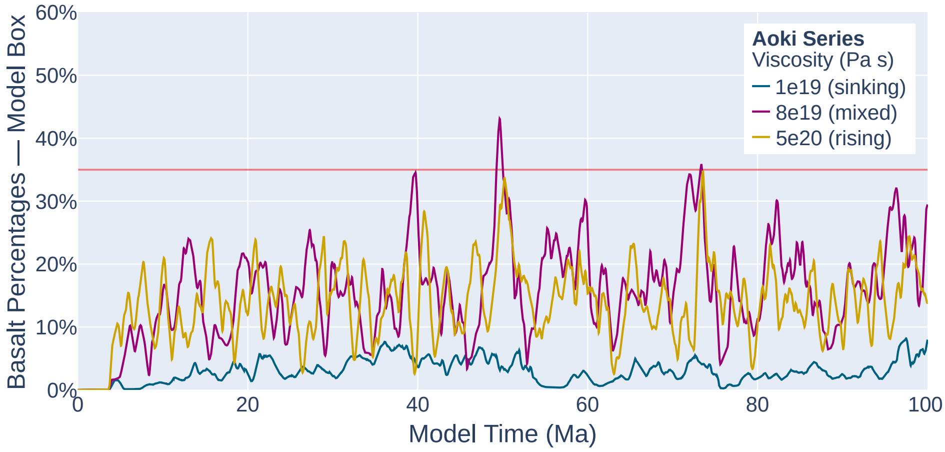

Figure 5. Evolution of the basalt fraction for three selected models in the Aoki series, all with a basalt inflow percentage of 15%. The model with a pyrolite viscosity of 8×10^{19} Pa s (mixed regime) shows the highest peak in the basalt fraction, reaching 40% at 50 Myr. The 5×10^{20} Pa s model (rising regime) displays a similar pattern, but has lower peaks of basalt fraction (up to approximately 32%), while the 10^{19} Pa s model (sinking regime) shows the lowest basalt percentage.

We note that basalt fractions comparable to the maximum values indicated by the regime diagrams (Figure 4) are only reached over short time intervals. Peaks in accumulation are followed by troughs, and throughout the majority of the model time, the basalt fractions remain consistently lower than these peaks, closer to the prescribed influx percentage.

To provide more context to our results in relation to the observations of Kemp et al. (2019), we further analyzed this evolution of the dynamically consistent models in the mixed regime. By integrating the time the basalt fraction exceeded 35%, we obtained the statistical probability of accumulating enough basaltic material for the X-discontinuity to be seismically visible at any given point in time (Figure 6). The threshold was chosen to be 35% as this is sufficiently close to the 40–50% of basalt estimated by Kemp et al. (2019) for the Hawaiian hotspot. This accounts for uncertainties in the seismic response to mineral phase transitions as evidenced by the discrepancy in amplitudes between receiver functions of different frequencies (Kemp et al., 2019; Pugh et al., 2021). Furthermore, 35% allows us to take into account a more substantial number of models in our analysis, with at least one model for each series.

The center panel of Figure 6 shows the results for a basalt influx of 20%. For the Hefesto series, the basalt fraction exceeds 35% only briefly – the probabilities are 1.19 and 0.55%, respectively. In the Aoki series, the lower density contrast between basalt and pyrolite greatly increases the probabilities. We find the highest probability ($\sim$5%) of large basalt fractions in the middle of the mixed regime, for a pyrolite viscosity of 6×10^{19} Pa s. The probability decreases to approximately 3% for lower and higher viscosity values, and sinks to 1% for a pyrolite viscosity of 3×10^{19} Pa s.

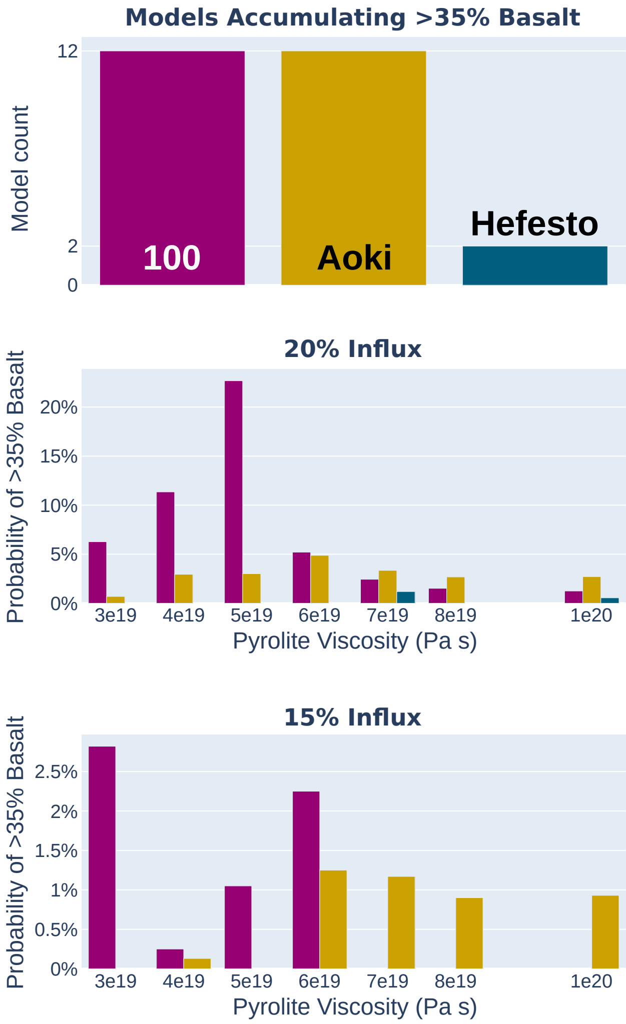

Figure 6. Statistical probability of dynamically consistent models to accumulate more than 35% basalt at any given point in time. The top panel shows the number of models reaching this basalt fraction. The middle and bottom panel display the probability in individual models with 20% and 15% basalt influx, respectively.

The 100 series displays ever higher probabilities. Basalt accumulation is most consistent for pyrolite viscosities of 3×10^{19} and 4×10^{19} Pa s. In these two cases, the probability of reaching more than 35% is the highest out of all models, and amounts respectively to 11.35 and 22.68%. The probability then gradually declines towards the edges of the mixed regime. These results highlight that basalt accumulates more consistently at the Ol–Wd transition compared to the coesite-stishovite transition (see also Sections 3.3 and 4).

The models with influx percentages of 15% show similar trends (Figure 6, right panel). In this case, only models from the 100 and Aoki series reach 35% of basalt, and the probabilities are about an order of magnitude lower than for the basalt inflow of 20%. Regardless of the series, none of the models featuring a 10% basalt influx accumulate more than 35%. However, many models come close to peaks of 30%.

3.3 Influence of the density

The second relevant factor determining the model evolution is the density contrast between the basaltic material and the background (Section 2.3). To illustrate its influence, we analyze the variability of the basalt fraction over time for a range of models (see Figure 7).

As expected, the basalt percentages reaching the phase transition are lowest for the lowest viscosities (sinking regime, top row of Figure 7). For viscosities of 10^{18} Pa s and 5×10^{18} Pa s (latter not shown), values never exceed 2%. This effect is mostly independent of the density.

The models in the mixed regime (yellow background in Figure 7) show the strongest differences between the three series, in particular for pyrolite viscosities of 3×10^{19} (second row from the top). Again, the 100 series reaches the highest fractions of basalt, the Hefesto series features the lowest fraction, and the Aoki series falls between the other two. The relative percentage difference between the 100 and Hefesto series, for the same basalt influx and pyrolite viscosity, reaches values as high as 77%, which is a direct consequence of the basalt density. The 100 series features a density difference of 70 kg/m^3 between pyrolite and the denser heterogeneities in the bottom half of the box, while the difference in the Hefesto series is twice as high (140 kg/m^3). The Aoki series shows an intermediate behavior, as the density difference between basalt and pyrolite is 100 kg/m^3.

Consequently, the Hefesto series also reaches its maximum basalt concentrations at higher viscosities compared to the other two series, especially the 100 series, and systematically attains basalt percentages which are on average 5 to 7% lower compared to similar runs in the other series. All models in the mixed regime also show punctual peaks in the basalt fraction, exceeding 40% for some models with basalt influx of 20% and 15%.

For increasingly high pyrolite viscosities in the mixed regime (rows 3 and 4 of Figure 7), the over time trends gradually become more similar between the series, such that there is a significant amount of overlap between the three curves. The 100 series shows slight decreases in the basalt quantities at viscosities higher than 8×10^{19}, while the Aoki and Hefesto series reach the highest basalt fractions around pyrolite viscosities of 8×10^{19} and 10^{20} Pa s.

Rows 5 and 6 of Figure 7 show two models in the rising regime. In these models, the differences between the series have disappeared completely, to the point that three curves are not individually distinguishable. These observations reflect the inherent characteristics of the rising regime. As the velocity of the heterogeneities is very close to the value prescribed as boundary condition, and the pyrolite viscosity is high enough

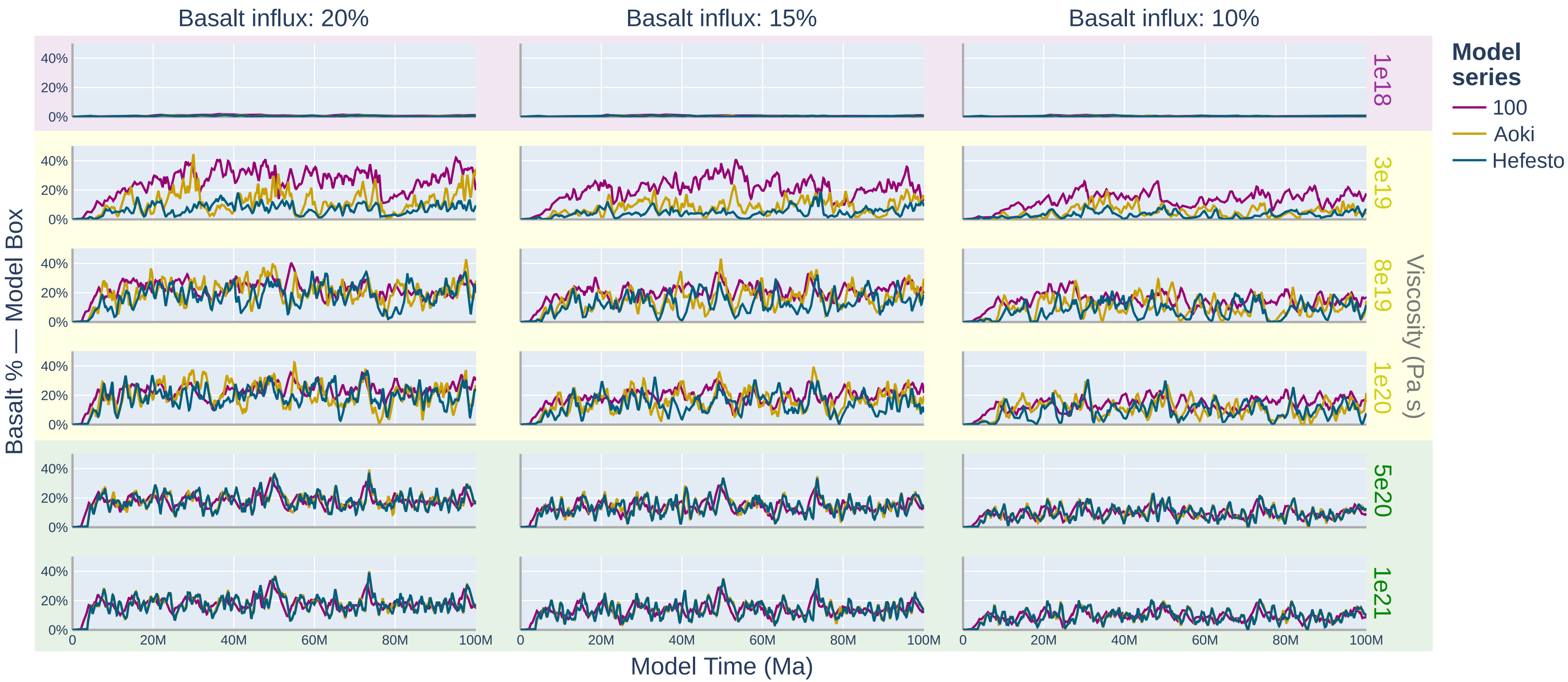

Figure 7. Evolution of the basalt fraction over time for selected pyrolite viscosity values (row numbers, right hand side) and basalt influx (columns). The background color scheme is the same as in Figure 4, with purple identifying the sinking regime, yellow the mixed regime, and green the rising regime. Only the three dynamically consistent influxes are shown (from left to right: 20%, 15%, and 10%).

to carry the denser material, the heterogeneities are transported with the same speed in all models and very little differences exist between them. At the highest viscosity (row 6), differences of the 100 series compared to the other models are mainly caused by the different depth ranges we use for averaging the basalt fraction. The basalt fractions in the Aoki and Hefesto series evolve almost identically.

4 Discussion

While previous studies indicated that plumes can carry no more than 15-20% denser material on their way through the mantle, our results show that there is a range of conditions under which much larger factions of basalt can accumulate within a plume conduit that on average carries about 15-20% of basalt. The highest amount of basalt in the depth range between 310 and 510 km for the 100 series, and between 260 and 360 km depth for the Aoki and Hefesto series, is attained for intermediate viscosity values that define the mixed regime. Specifically, assuming a radius of 17.5 km for the heterogeneities, pyrolite viscosities of at least $2-3\times10^{19}$ Pa s, but not more than $1-2\times10^{20}$ Pa s are required for the material to pond between the Ol–Wd and Co–St phase transitions. Slightly lower maximum basalt fractions are attained for higher viscosities in the rising regime.

Although our models feature high percentages of basalt near the Co–St transition both in the mixed and the rising regime, the underlying mechanisms are fundamentally different. Notably, the amount of basalt does not remain constant throughout the model evolution (Figure 5). Instead, it varies statistically around the influx percentage and displays highs and lows. This variation is caused by two concurrent mechanisms.

In all models, the statistical variations in the distribution of the basaltic heterogeneities—which flow into the model at random locations—causes cyclical highs and lows in the amount of basalt at a given depth. On the length scale of the seismologic resolution, these variations can lead to maximum basalt fractions in the plume of more than double of the influx percentage of basalt. Consequently, even if heterogeneities do not pond and accumulate, such as in the rising regime, the absolute percentages of basalt fraction at a given point in time might still exceed the average amount of basalt within the plume.

In the mixed regime, there is an additional mechanism that leads to increased basalt fractions: Basaltic material ponds in the depth range between the two discontinuities. Accordingly, the residence time of the heterogeneities within the plume conduit increases and they can accumulate. This effect is not as strong as the statistical variation, however, it increases not just the peaks, but also the temporal average of the basalt fraction at a given depth. The combination of the two effects leads to overall higher percentages of basalt of 35-40% or more even for basalt influxes of 20% or less. Consequently, the distribution of basalt in the mixed regime can best explain the seismological observations.

The effect of the two competing mechanisms is illustrated in Figure 8, which shows different models of the mixed regime. While the basalt fraction varies over time, its time average is also slightly higher than the basalt influx, indicating the accumulation of basalt around the phase transition. This effect is most pronounced in the 100 series (left column), where the time-averaged basalt fraction can be 5-10% larger than the amount of basalt flowing in. The Aoki series (center column) shows this effect to a lesser extent, and in the Hefesto series (right column) the average and influx basalt fractions are comparable. In the rising regime (not shown) this effect is absent and the model average is equal to the basalt influx.

With regards to the modeled phase transitions, these results highlight the importance of the Ol–Wd transition for the accumulation of basalt. At this transition,

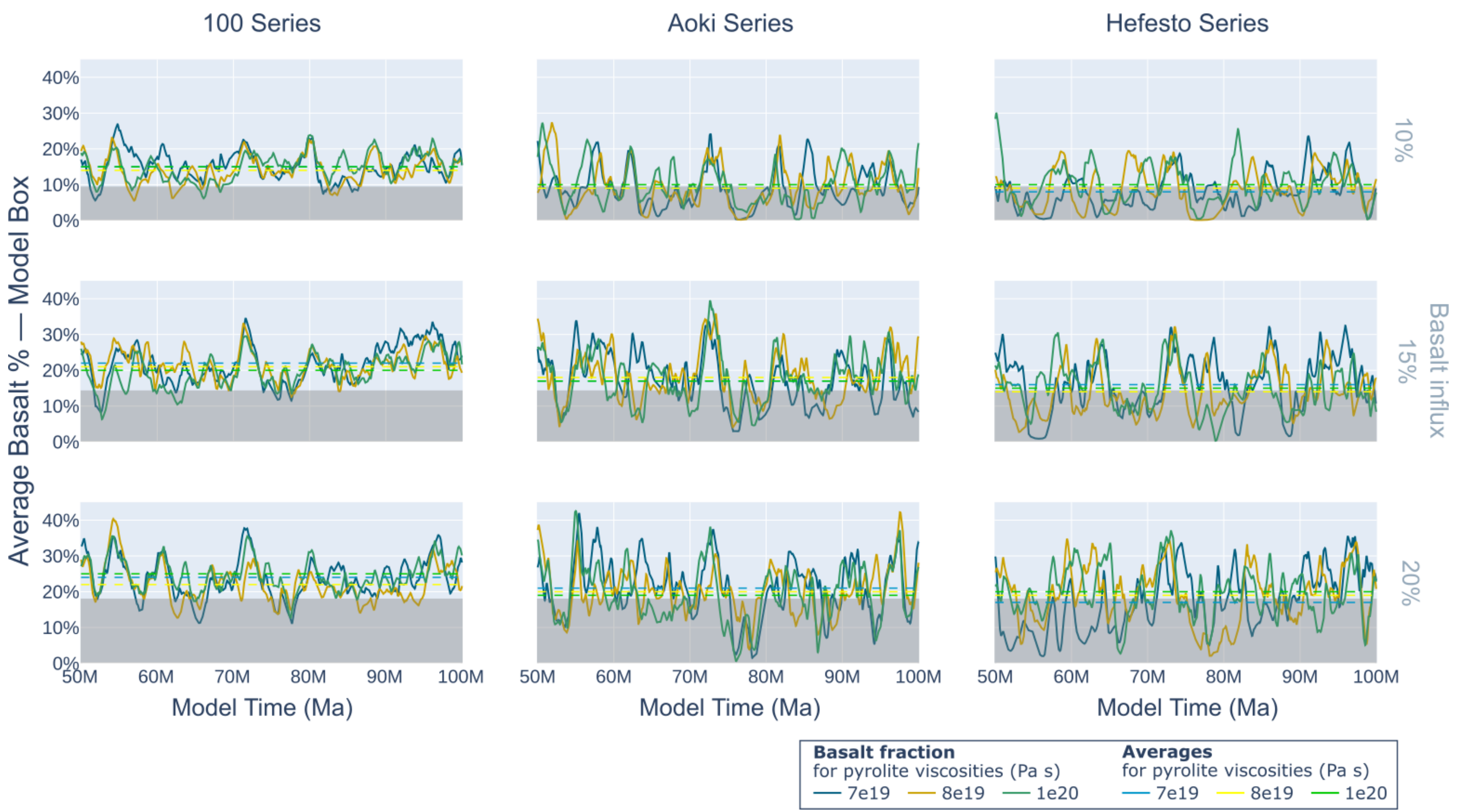

Figure 8. Evolution of the basalt fraction over time (as in Figure 7, solid lines) and average basalt fraction (dashed horizontal lines) for three selected pyrolite viscosities (darker colors in the legend). The gray boxes indicate the basalt influx percentages, as indicated to the right of each row. The different columns refer to the three different model series. The 100 series shows the most marked basalt accumulation, while the Hefesto series displays the least average basalt with respect to the influx.

the heterogeneities slow down as a consequence of the increased density contrast above 410 km depth, and our models predict the strongest effect of hovering. This explains why the effect is strongest in the 100 series, where we average in a depth range of 310 to 510 km, around the Ol–Wd transition. In contrast, the average basalt fractions in the Aoki and Hefesto series (depth range of 260 to 360 km, around the X-discontinuity) are only slightly higher than the influx. The Co–St transition, on the other hand, does not play a primary role for the model dynamics. Even the models of the 100 series that do not include this additional transition show substantial accumulation of basalt.

4.1 Implications for the Hawaiian mantle plume

Our observations only partially corroborate the findings in Kemp et al. (2019). The authors tentatively explain the suppression of the 410 km depth discontinuity beneath the Big Island of Hawaii with the occurrence of extremely high quantities of basaltic material, up to 60-70%. While we observe the strongest effect of ponding directly above 410 km depth, we never observe more than 45% basaltic material, assuming physically feasible influx percentages. It may however be possible that locally, more than 45% basalt accumulates within the mantle plume. Our models average the fraction of basalt over the whole cross section of the plume conduit, whereas the receiver functions beneath the Big Island of Hawaii indicate the vanishing of the 410 km discontinuity only for a part of the plume. Consequently, a large accumulation of basaltic heterogeneities on the length scale of the resolution of the study of Kemp et al. (2019) ($\sim$100 km) might explain this observation.

It remains challenging to reconcile the observation of the X-discontinuity in multiple plume locations (Pugh et al., 2021). With the time-varying nature of the basalt fraction in our models, it is implausible that so many plumes have concentrations of basalt above the 40% threshold required for seismic observation. However, several seismic studies attribute their observations to two, or more, causal mechanisms (Bagley & Revenaugh, 2008; Pugh et al., 2021).

4.2 Model limitations

In order to analyze and observe the behavior of the basaltic heterogeneities, we have made several simplifying assumptions.

First, the dynamics of our models does not take into account the influence of temperature or compressibility. In the Earth's mantle, a plume would rise with a variable velocity, depending both on its temperature compared to the surrounding material and its chemical composition. Phase transitions would occur at a variable depth depending on their Clapeyron slope and the temperature distribution within the plume conduit, introducing additional variations in buoyancy. In contrast, our models prescribe a constant rising velocity for the modeled section of the plume, only taking into account compositional density variations. This means that the flow in our modeled plume conduit is still dominantly upwards, even if the negative buoyancy introduced by the dense basaltic heterogeneities exceeds the positive buoyancy due to the high plume temperatures. Consequently, we rely on existing studies (e.g., Dannberg & Sobolev, 2015) to constrain the maximum amount of basalt that plumes can carry towards the surface and to identify which of our models are applicable to plumes in the Earth's mantle (see *dynamically consistent* models, Figure 4).

Another simplification is the model geometry. Because our side boundaries are closed, plume material is constrained in its horizontal motion, fixing the shape of the plume conduit. In the Earth, one would expect that plume material that is cyclically rising and sinking at 300-400 km depth would move laterally, away from the center of the plume conduit. This may lead to the accumulation of a large amount of basaltic material around the plume conduit (similar to a deep eclogitic pool Ballmer et al., 2013). On the other hand, the basaltic material is likely to sink downwards as soon as it has moved laterally and is no longer supported by the upwards flow within the plume conduit. Plume material would also be deflected to the side when reaching the base of the lithosphere, which we did not include in our models. How exactly the results would change remains an open question to be answered in future studies. However, we believe our main conclusion—that locally, more than 35-40% of basalt can accumulate in plume conduits despite its large density—remains unaffected by this assumption.

Uncertainty in our models also comes from the mantle composition. We here assume that the background mantle material has a pyrolitic composition. However, seismological studies (Cammarano et al., 2009; Ritsema et al., 2009; Xu et al., 2008) show that in the mantle transition zone, mineral physics predictions fit observed seismic velocities overall better when taking into account a mechanical mixture of basalt and harzburgite compared to a pyrolitic equilibrium assemblage.

Depending on the length scale of heterogeneities in the mechanical mixture, the background mantle composition within the plume could also be harzburgitic, or it could be a mechanical mixture, with basalt and harzburgite being mixed on a much smaller length scale than the diameter of $30 - 40$ km we assume for our basaltic heterogeneities. Both possibilities would affect the model predictions. The small-scale mechanical mixture would have a similar density profile as the one we use for pyrolite, so the effect on the model dynamics is likely to be small. However, it would contain some free SiO_2, increasing the effective total amount of coesite/stishovite in the plume and making the detection of the X-discontinuity more likely, even with basalt fractions slightly less than 40%. If the background composition would be harzburgitic, that would slightly increase the density contrast between the basaltic heterogeneities and the background, shifting all regimes to slightly higher viscosities. But it would also make the plume overall less dense, allowing it to carry slightly more recycled basaltic material while still being positively buoyant, and therefore allowing larger basalt influx percentages.

5 Conclusions

We simulate the ascent of dense chemical heterogeneities within a plume conduit to determine the maximum percentages of basaltic material that can accumulate within a rising mantle plume in the depth around the Ol–Wd and Co–St phase transitions. Our results show that, even for basalt influx percentages lower than 20%—consistent with constraints from earlier geodynamic studies—the basalt fraction in a mantle plume can reach peaks of 40% or more. Our study demonstrates that basalt can accumulate within a plume conduit to much higher fractions than previously thought. It also provides a viable mechanism explaining the underlying dynamics that lead to the seismic observations of the X-discontinuity in the mid-upper mantle beneath the Hawaiian hotspot.

We also explored the conditions under which denser material can accumulate. Our models show that there are two fundamentally different underlying mechanisms that can lead to large fractions of basalt within the plume conduit. On the one hand, basalt ponds above the Ol–Wd transition. This is an effect of the interplay between downwards gravity forces—which are enhanced at this depth because the density contrast between basalt and pyrolite is largest—and frictional forces due the upwards motion within the plume conduit. On the other hand, statistical variations due to the random distribution of the basaltic heterogeneities cause cyclical highs and lows in the amount of basalt at any given depth. The latter effect is stronger in our models. On the length scale of the seismologic resolution, statistical variations can lead to maximum basalt fractions of more than double of the average amount of basalt in the plume. Conversely, ponding of heterogeneities only increases the basalt fraction by about one third to half of the amount of basalt being carried upwards from the lower mantle, and is strongest around the depth of the Ol–Wd transition.

For a diameter of the basaltic heterogeneities of 30–40 km, the strongest accumulation of denser material occurs when the pyrolite viscosity is between 3×10^{19} and 1×10^{20} Pa s, a range that encompasses our mixed regime. At lower values, only little basalt is entrained into the upwards flow. Higher values do not allow for the heterogeneities to move relative to the rest of the plume. Therefore, basalt can not accumulate and high percentages are only due to statistical variations. Since the statistical effect of basalt accumulation is dominant, high values of 35–40% or more cannot be sustained for a prolonged amount of time. Under the most favorable circumstances (a basalt influx of 20%, a viscosity of 6×10^{19}, and using densities from Aoki and Takahashi (2004)), the basalt fraction at ∼300 km depth exceeds 35% for about 5% of the time.

Further research is needed to investigate if lateral spreading of the material ponding above the Ol–Wd transition could increase the accumulation effect and how plume dynamics would be affected by the large basalt fractions.

Appendix A Velocity Diagrams

Figure A1 shows the maximum value of root mean square of the velocity, averaged over the depth range of interest, attained in each model. As outlined in Section 3.1, we used these values to define the boundary between the mixed and rising regimes. The prescribed boundary velocity is 0.1 m/yr, a value that corresponds to the absence of deformation. Since deformation is minimal in the rising regime, models in this regime have a root mean square velocity that is close to 0.1 m/yr. We therefore classify a model as being in the mixed regime (or sinking regime) if its average velocity in the depth range of interest for each of the three series exceeds 0.12 m/yr at any point in time. Mixed and sinking regime are distinguished based on their basalt fraction (Section 3.1).

Acknowledgments

Computations were done using the ASPECT code version 2.4.0-pre (commit c1c5a8a95). We thank the Computational Infrastructure for Geodynamics (geodynamics.org), which is funded by the National Science Foundation under award EAR-0949446 and EAR-1550901 for supporting the development of ASPECT. JD and RG were partially supported by the NSF grants EAR-1925677 and EAR-2054605. The authors acknowledge University of Florida Research Computing (http://rc.ufl.edu) for providing computational resources and support that have contributed to the research results reported in this publication.

All software and data used to generate the results and figures in this manuscript are freely available. The specific files and instructions are published as a Zenodo data package (http://doi.org/10.5281/zenodo.6687407) and include the source code and links to the GitHub versions of ASPECT as well as the input files to compute the models and plotting scripts to generate the figures.

References

Aoki, I., & Takahashi, E. (2004). Density of morb eclogite in the upper mantle. *Physics of the Earth and Planetary Interiors*, *143*, 129–143.

Arndt, D., Bangerth, W., Davydov, D., Heister, T., Heltai, L., Kronbichler, M., ... Wells, D. (2021). The deal.II finite element library: Design, fea-

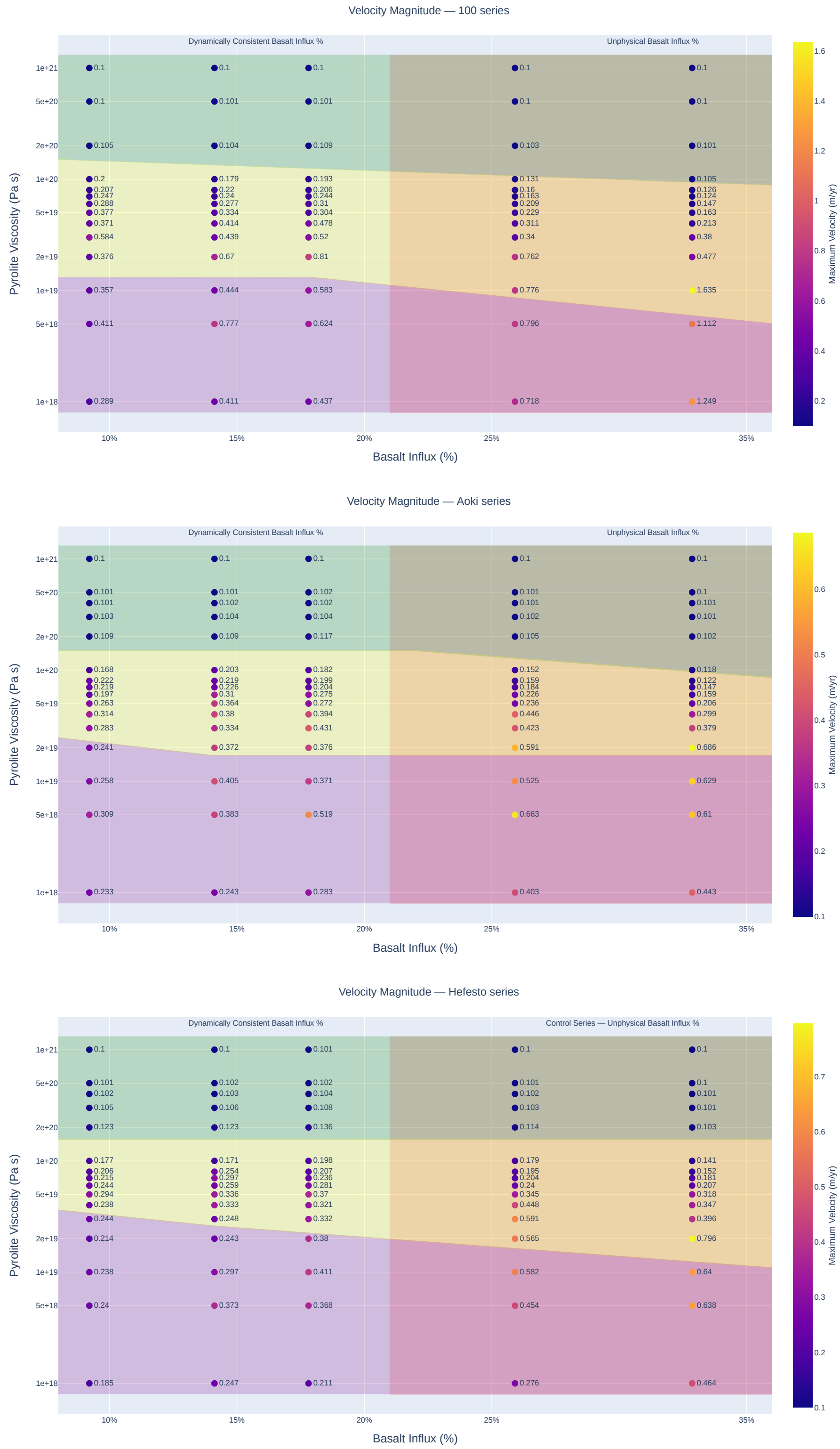

Figure A1. Velocity diagrams for the three series. The color of each point and the value next to it indicate the root mean square velocity in the model, averaged in the depth range of interest (between 260 and 360 km mantle depth in the Aoki and Hefesto series, and between 310 and 510 km depth in the 100 series). The background colors are the same as in the respective regime diagrams (Figure 3), and indicate, from bottom to top: the sinking regime (purple), the mixed regime (yellow), and the rising regime (green).

tures, and insights. *Computers & Mathematics with Applications*, *81*, 407-422. Retrieved from https://arxiv.org/abs/1910.13247 doi: 10.1016/j.camwa.2020.02.022

Bagley, B., & Revenaugh, J. (2008). Upper mantle seismic shear discontinuities of the pacific. *Journal of Geophysical Research: Solid Earth*, *113*(B12).

Ballmer, M. D., Ito, G., Wolfe, C. J., & Solomon, S. C. (2013). Double layering of a thermochemical plume in the upper mantle beneath hawaii. *Earth and Planetary Science Letters*, *376*, 155–164.

Bangerth, W., Dannberg, J., Fraters, M., Gassmoeller, R., Glerum, A., Heister, T., & Naliboff, J. (2021a, July). ASPECT*: Advanced Solver for Problems in Earth's ConvecTion, User Manual.* Retrieved from https://doi.org/10.6084/m9.figshare.4865333 (doi:10.6084/m9.figshare.4865333) doi: 10.6084/m9.figshare.4865333

Bangerth, W., Dannberg, J., Fraters, M., Gassmoeller, R., Glerum, A., Heister, T., & Naliboff, J. (2021b, July). *Aspect v2.3.0* [software]. Zenodo. Retrieved from https://doi.org/10.5281/zenodo.5131909 doi: 10.5281/zenodo.5131909

Burstedde, C., Wilcox, L. C., & Ghattas, O. (2011). p4est: Scalable algorithms for parallel adaptive mesh refinement on forests of octrees. *SIAM Journal on Scientific Computing*, *33*(3), 1103-1133. doi: 10.1137/100791634

Cammarano, F., Romanowicz, B., Stixrude, L., Lithgow-Bertelloni, C., & Xu, W. (2009, 11). Inferring the thermochemical structure of the upper mantle from seismic data. *Geophysical Journal International*, *179*(2), 1169-1185. Retrieved from https://doi.org/10.1111/j.1365-246X.2009.04338.x doi: 10.1111/j.1365-246X.2009.04338.x

Chen, T., Liebermann, R. C., Zou, Y., Li, Y., Qi, X., & Li, B. (2017). Tracking silica in earth's upper mantle using new sound velocity data for coesite to 5.8 gpa and 1073 k. *Geophysical Research Letters*, *44*(15), 7757–7765.

Christensen, U. R., & Hofmann, A. W. (1994). Segregation of subducted oceanic crust in the convecting mantle. *Journal of Geophysical Research: Solid Earth*, *99*(B10), 19867–19884.

Courtier, A. M., Bagley, B., & Revenaugh, J. (2007, September). Whole mantle discontinuity structure beneath hawaii. *Geophysical Research Letters*, *34*(17). Retrieved from https://doi.org/10.1029/2007gl031006 doi: 10.1029/2007gl031006

Dannberg, J., & Sobolev, S. V. (2015). Low-buoyancy thermochemical plumes resolve controversy of classical mantle plume concept. *Nature communications*, *6*(1), 1–9.

Deuss, A., & Woodhouse, J. H. (2002). A systematic search for mantle discontinuities using ss-precursors. *Geophysical Research Letters*, *29*(8), 90–1.

Eiler, J. M., Farley, K. A., Valley, J. W., Hofmann, A. W., & Stolper, E. M. (1996). Oxygen isotope constraints on the sources of hawaiian volcanism. *Earth and Planetary Science Letters*, *144*(3-4), 453–467.

Faccenda, M., & Dal Zilio, L. (2017). The role of solid–solid phase transitions in mantle convection. *Lithos*, *268*, 198–224.

Farla, R., Rosenthal, A., Bollinger, C., Petitgirard, S., Guignard, J., Miyajima, N., ... Frost, D. J. (2017). High-pressure, high-temperature deformation of dunite, eclogite, clinopyroxenite and garnetite using in situ x-ray diffraction. *Earth and Planetary Science Letters*, *473*, 291–302.

Farnetani, C., & Samuel, H. (2005). Beyond the thermal plume paradigm. *Geophysical Research Letters*, *32*(7).

Gassmöller, R., Lokavarapu, H., Bangerth, W., & Puckett, E. G. (2019). Evaluating the accuracy of hybrid finite element/particle-in-cell methods for modelling incompressible stokes flow. *Geophysical Journal International*, *219*(3), 1915–1938.

Gassmöller, R., Lokavarapu, H., Heien, E., Puckett, E. G., & Bangerth, W. (2018).

Flexible and scalable particle-in-cell methods with adaptive mesh refinement for geodynamic computations. *Geochemistry, Geophysics, Geosystems*, *19*(9), 3596–3604.

Hauri, E. H. (1996). Major-element variability in the hawaiian mantle plume. *Nature*, *382*(6590), 415–419.

Heister, T., Dannberg, J., Gassmöller, R., & Bangerth, W. (2017). High accuracy mantle convection simulation through modern numerical methods. II: Realistic models and problems. *Geophysical Journal International*, *210*(2), 833-851. Retrieved from https://doi.org/10.1093/gji/ggx195 doi: 10.1093/gji/ggx195

Hofmann, A. W., & White, W. M. (1982). Mantle plumes from ancient oceanic crust. *Earth and Planetary Science Letters*, *57*(2), 421–436.

Jacobsen, S. D., Liu, Z., Ballaran, T. B., Littlefield, E. F., Ehm, L., & Hemley, R. J. (2010). Effect of h2o on upper mantle phase transitions in mgsio3: Is the depth of the seismic x-discontinuity an indicator of mantle water content? *Physics of the Earth and Planetary Interiors*, *183*(1-2), 234–244.

Jellinek, A. M., & Manga, M. (2004). Links between long-lived hot spots, mantle plumes, d", and plate tectonics. *Reviews of Geophysics*, *42*(3).

Jin, Z.-M., Zhang, J., Green, H., & Jin, S. (2001). Eclogite rheology: Implications for subducted lithosphere. *Geology*, *29*(8), 667–670.

Kemp, M., Jenkins, J., Maclennan, J., & Cottaar, S. (2019). X-discontinuity and transition zone structure beneath hawaii suggests a heterogeneous plume. *Earth and Planetary Science Letters*, *527*, 115781.

Kronbichler, M., Heister, T., & Bangerth, W. (2012, 10). High accuracy mantle convection simulation through modern numerical methods. *Geophysical Journal International*, *191*(1), 12-29. Retrieved from https://doi.org/10.1111/j.1365-246X.2012.05609.x doi: 10.1111/j.1365-246X.2012.05609.x

Kumagai, I., Davaille, A., Kurita, K., & Stutzmann, E. (2008). Mantle plumes: Thin, fat, successful, or failing? constraints to explain hot spot volcanism through time and space. *Geophysical Research Letters*, *35*(16).

Lin, S.-C., & van Keken, P. E. (2006). Dynamics of thermochemical plumes: 1. plume formation and entrainment of a dense layer. *Geochemistry, Geophysics, Geosystems*, *7*(2).

Lin, S.-C., & Van Keken, P. E. (2006). Dynamics of thermochemical plumes: 2. complexity of plume structures and its implications for mapping mantle plumes. *Geochemistry, Geophysics, Geosystems*, *7*(3).

Manga, M. (1996). Mixing of heterogeneities in the mantle: Effect of viscosity differences. *Geophysical Research Letters*, *23*(4), 403–406.

Pugh, S., Jenkins, J., Boyce, A., & Cottaar, S. (2021, May). Global receiver function observations of the x-discontinuity reveal recycled basalt beneath hotspots. *Earth and Planetary Science Letters*, *561*, 116813. Retrieved from https://doi.org/10.1016/j.epsl.2021.116813 doi: 10.1016/j.epsl.2021.116813

Revenaugh, J., & Jordan, T. H. (1991). Mantle layering from scs reverberations: 3. the upper mantle. *Journal of Geophysical Research: Solid Earth*, *96*(B12), 19781–19810.

Ritsema, J., Xu, W., Stixrude, L., & Lithgow-Bertelloni, C. (2009). Estimates of the transition zone temperature in a mechanically mixed upper mantle. *Earth and Planetary Science Letters*, *277*(1), 244-252. Retrieved from https://www.sciencedirect.com/science/article/pii/S0012821X08006845 doi: https://doi.org/10.1016/j.epsl.2008.10.024

Samuel, H., & Bercovici, D. (2006). Oscillating and stagnating plumes in the earth's lower mantle. *Earth and Planetary Science Letters*, *248*(1-2), 90–105.

Schmerr, N. C., Kelly, B. M., & Thorne, M. S. (2013). Broadband array observations of the 300 km seismic discontinuity. *Geophysical Research Letters*, *40*(5), 841–846.

Schubert, G., Turcotte, D. L., & Olson, P. (2001). *Mantle convection in the earth and planets*. Cambridge University Press. doi: 10.1017/CBO9780511612879

Sobolev, A. V., Hofmann, A. W., Kuzmin, D. V., Yaxley, G. M., Arndt, N. T., Chung, S.-L., ... others (2007). The amount of recycled crust in sources of mantle-derived melts. *science*, *316*(5823), 412–417.

Sobolev, A. V., Hofmann, A. W., Sobolev, S. V., & Nikogosian, I. K. (2005). An olivine-free mantle source of hawaiian shield basalts. *Nature*, *434*(7033), 590–597.

Sobolev, S. V., Sobolev, A. V., Kuzmin, D. V., Krivolutskaya, N. A., Petrunin, A. G., Arndt, N. T., ... Vasiliev, Y. R. (2011). Linking mantle plumes, large igneous provinces and environmental catastrophes. *Nature*, *477*(7364), 312–316.

Stixrude, L., & Lithgow-Bertelloni, C. (2011). Thermodynamics of mantle minerals-ii. phase equilibria. *Geophysical Journal International*, *184*(3), 1180–1213.

Tackley, P. J. (2007). Mantle geochemical geodynamics. *Treatise on Geophysics*, *7*, 437–505.

Trilinos Project Team, T. (n.d.). The Trilinos Project Website [Computer software manual].

van Zelst, I., Crameri, F., Pusok, A. E., Glerum, A., Dannberg, J., & Thieulot, C. (2021). 101 geodynamic modelling: How to design, carry out, and interpret numerical studies. *Solid Earth Discussions*, *2021*, 1–80. Retrieved from `https://se.copernicus.org/preprints/se-2021-14/` doi: 10.5194/se-2021-14

Williams, Q., & Revenaugh, J. (2005). Ancient subduction, mantle eclogite, and the 300 km seismic discontinuity. *Geology*, *33*(1), 1–4.

Woodland, A. B. (1998). The orthorhombic to high-p monoclinic phase transition in mg-fe pyroxenes: Can it produce a seismic discontinuity? *Geophysical Research Letters*, *25*(8), 1241–1244.

Woodland, A. B., & Angel, R. J. (1997). Reversal of the orthoferrosilite-high-p clinoferrosilite transition, a phase diagram for fesio3 and implications for the mineralogy of the earth's upper mantle. *European Journal of Mineralogy*, 245–254.

Xu, W., Lithgow-Bertelloni, C., Stixrude, L., & Ritsema, J. (2008). The effect of bulk composition and temperature on mantle seismic structure. *Earth and Planetary Science Letters*, *275*(1-2), 70–79.